

# A non-Hermitian Su-Schrieffer-Heeger model with the energy levels of free parafermions

Edward McCann\*

*Department of Physics, Lancaster University, Lancaster, LA1 4YB, United Kingdom*

Using a parent Hermitian tight-binding model on a bipartite lattice with chiral symmetry, we theoretically generate non-Hermitian models for free fermions with  $p$  orbitals per unit cell satisfying a complex generalization of chiral symmetry. The  $p$  complex energy bands in  $k$  space are given by a common  $k$ -dependent real factor, determined by the bands of the parent model, multiplied by the  $p$ th roots of unity. When the parent model is the Su-Schrieffer-Heeger (SSH) model, the single-particle energy levels are the same as those of free parafermion solutions to Baxter's non-Hermitian clock model. This construction relies on fully unidirectional hopping to create Bloch Hamiltonians with the form of generalized permutation matrices, but we also describe the effect of partial unidirectional hopping. For fully bidirectional hopping, the Bloch Hamiltonians are Hermitian and may be separated into even and odd parity blocks with respect to inversion of the orbitals within the unit cell. Partially unidirectional hopping breaks the inversion symmetry and mixes the even and odd blocks, and the real energy spectrum evolves into a complex one as the degree of unidirectionality increases, with details determined by the topology of the parent model and the number of orbitals per unit cell,  $p$ . We describe this process in detail for  $p = 3$  and  $p = 4$  with the SSH model. We also apply our approach to graphene, and show that AA-stacked bilayer graphene evolves into a square root Hamiltonian of monolayer graphene with the introduction of unidirectional hopping. We show that higher-order exceptional points occur at edge states and solitons in the non-Hermitian SSH model, and at the Dirac point of non-Hermitian graphene.

## I. INTRODUCTION

The Su-Schrieffer-Heeger (SSH) model [1–3] is an Hermitian tight-binding model of noninteracting spinless fermions in one dimension with staggered nearest-neighbor hopping and two orbitals per unit cell. It satisfies time-reversal, charge-conjugation and chiral symmetries, placing it in the BDI class of topological insulators [4–7]. Non-Hermitian SSH models have been considered by adding additional tight-binding parameters, usually in one of two ways. The first is to add alternating complex onsite energies which break chiral symmetry but satisfy parity-time (PT) symmetry and may preserve a real energy eigenvalue spectrum [8–18]. The second approach is to add terms which introduce unidirectional hopping [19–25], an imbalance in the left-moving and right-moving hopping parameters, breaking PT symmetry but preserving chiral symmetry [15–17, 26–28]. Novel phenomena include exceptional points and the non-Hermitian skin effect [13, 15–17, 27–43].

In this paper, we consider non-Hermitian Hamiltonians for non-interacting fermions which satisfy a complex generalization of chiral symmetry [44–46] expressed, for a Bloch Hamiltonian  $\mathcal{H}(k)$  in  $k$  space, as

$$Z\mathcal{H}(k)Z^{-1} = \omega\mathcal{H}(k), \quad \omega = \exp(2\pi i/p), \quad (1)$$

where  $p \geq 2$  is an integer. This chiral symmetry guarantees that the energy spectrum separates into  $p$  sectors, and bands in different sectors are related by a common real part multiplied by the  $p$ th roots of unity.

For simplicity, we consider  $p$  orbitals per unit cell so that  $\mathcal{H}(k)$  is a  $p \times p$  matrix with  $p$  energy bands, and the chiral operator  $Z$  is a  $p \times p$  generalization of the diagonal Pauli matrix,  $Z = \text{diag}(1, \omega, \omega^2, \dots, \omega^{p-1})$ . Then, the chiral symmetry (1) may generally be satisfied with  $\mathcal{H}(k)$  in the form of a generalized permutation matrix [45] containing  $p$  independent functions of  $k$ . Instead of a general Hamiltonian, however, we propose a theoretical scheme to generate the non-Hermitian models from parent Hermitian models on a bipartite lattice. By introducing unidirectional hopping [19–22] and increasing the number of orbitals to  $p$ , the  $p$  complex energy bands are given by a common  $k$ -dependent real factor, determined by the bands of the parent model, multiplied by the  $p$ th roots of unity.

An example where the parent model is the SSH model is illustrated in Fig. 1. Figure 1(a) shows the Hermitian SSH model with two orbitals per unit cell on sublattices  $A$  and  $B$  with intracell hopping  $t \geq 0$  and intercell hopping  $J \geq 0$ , where the hopping is bidirectional. The non-Hermitian SSH model with  $p = 3$  is shown in Fig. 1(b) where site  $B$  supports two orbitals,  $B1$  and  $B2$ , connected by unidirectional hopping  $\gamma > 0$ , with unidirectional hopping from  $A$  to  $B1$  and from  $B2$  to  $A$ . The unidirectional hopping is implemented so that it circulates in a counter-clockwise direction in every intracell trimer and in a clockwise direction in every intercell trimer, as if created by an imaginary gauge field [19–22]. For fully unidirectional hopping, the non-Hermitian model has an energy spectrum related to that of the parent SSH model, and, as with the parent SSH model [3], bulk-edge correspondence may be understood pictorially in the trimer limit. For  $t \neq 0, J = 0$ , Fig. 1(c), the system splits into separate trimers, each with energy  $\epsilon^3 = \gamma t^2$ , and

\* ed.mccann@lancaster.ac.uk

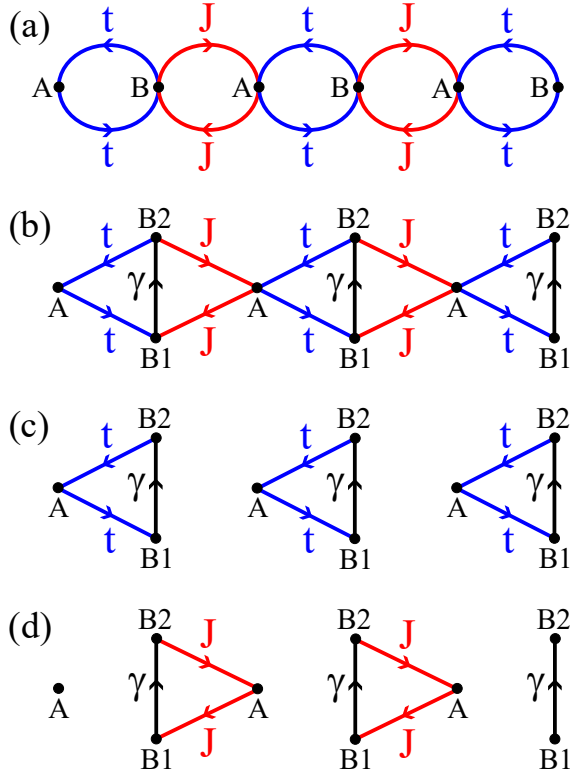


FIG. 1. (a) Hermitian SSH model with two orbitals per unit cell on sublattices  $A$  and  $B$  with intracell hopping  $t \geq 0$  and intercell hopping  $J \geq 0$ . (b) Non-Hermitian Hamiltonian formed from the parent SSH model with two orbitals  $B1$  and  $B2$  connected by unidirectional hopping  $\gamma > 0$  as indicated by the arrows, with unidirectional hopping from  $A$  to  $B1$  and from  $B2$  to  $A$ . (c) The topologically trivial phase in the trimer limit with  $J = 0$ , where each trimer has three states with energies  $\epsilon^3 = \gamma t^2$ . (d) The topologically nontrivial phase in the trimer limit with  $t = 0$ , where each trimer has three states with energies  $\epsilon^3 = \gamma J^2$ , and there are three edge states with energy  $\epsilon = 0$ .

there are no edge states (the trivial phase). However, for  $t = 0$ ,  $J \neq 0$ , Fig. 1(d), the system splits into separate trimers, each with energy  $\epsilon^3 = \gamma J^2$ , plus  $p = 3$  edge states with energy  $\epsilon = 0$  (the nontrivial phase): two at the right edge and one at the left edge. This is an exceptional point [13, 15–17, 27–43, 46]: The right edge supports a defective eigenvalue at zero energy with an algebraic multiplicity of two, as defined by the roots of the characteristic polynomial, but, owing to the unidirectional coupling of  $\gamma$  from  $B1$  to  $B2$ , there is only one linearly-independent eigenvector.

It is generally difficult to realize unidirectional hopping in electronic condensed matter systems [20–22]. However, there have been theoretical proposals and experimental realizations of partially unidirectional hopping in other platforms including optical [22, 46–54], acoustic [55–57], cold atom [58–60], and topoelectrical [61–63] systems. The non-Hermitian model with  $p = 3$  and the SSH model as the parent model, Fig. 1(b), bears some

similarity to the model discussed in Ref. [46] as a cube root of the SSH model, although their model has six sites per unit cell (instead of three) and different values of the unidirectional hopping parameters as compared to  $H^{(1,2)}$ . Ref. [46] proposes the implementation of their model using photonic ring resonators [22, 47, 49, 50, 52], and they estimate that it is possible to achieve very close to perfect unidirectionality. Motivated by these works on experimental realizations, we consider the influence of partially unidirectional hopping in Sec. III.

Section II details the construction of non-Hermitian Hamiltonians with  $p$  orbitals and fully unidirectional hopping which satisfy the complex chiral symmetry (1). We show that it is possible to construct an arbitrary  $n$ th root model of the parent [46, 50, 64–72] and we describe the occurrence of exceptional points [13, 15–17, 27–43, 46]. When the parent model is the SSH model, the single-particle energy levels in position space with open boundary conditions are the same as those of free parafermion solutions to Baxter’s non-Hermitian clock model [44, 73, 74].

Section III describes the role of partially unidirectional hopping which breaks the complex chiral symmetry (1). Nevertheless, the complex energy spectrum is constrained by time-reversal symmetry and, for an even number of orbitals  $p$ , by sublattice symmetry. For fully bidirectional hopping, the constructed model is Hermitian, and it can be block diagonalized into even and odd parity blocks with respect to inversion of the orbitals within the unit cell. Partially unidirectional hopping breaks the inversion symmetry and mixes the even and odd blocks, and the real energy spectrum evolves into a complex one as the degree of unidirectionality increases. This process is determined by the topology of the parent model and by the number of orbitals per unit cell,  $p$ , which we describe in detail for  $p = 3$  and  $p = 4$  with the example of the SSH model. When the SSH model is the parent model, there are real energy levels due to states localized at edges in the topological phase or localized on solitons.

Section IV considers the application to graphene [75–77]. For fully unidirectional hopping, it is possible to construct an arbitrary  $n$ th root Hamiltonian of graphene with exceptional points at the Dirac points characterized by  $2n$  complex bands with dispersion  $\epsilon \sim |\mathbf{q}|^{1/n}$  for small wave vector  $\mathbf{q}$  and Berry’s phase  $\pi$  [10, 78–82]. In particular, we show how the introduction of unidirectional hopping changes Hermitian  $AA$ -stacked bilayer graphene [83, 84] into a square root Hamiltonian of monolayer graphene.

## II. FULLY UNIDIRECTIONAL HOPPING

### A. General form of the non-Hermitian Bloch Hamiltonian

In this section, we describe the construction of the non-Hermitian model when the hopping is fully unidirectional. We consider a Hamiltonian  $H^{(m,n)}(u)$  for a system with  $m$  orbitals on the  $A$  site,  $A1, A2, \dots, Am$ ,  $n$  orbitals on the  $B$  site,  $B1, B2, \dots, Bn$ , and  $p = m + n$  orbitals per unit cell. The parameter  $0 \leq u \leq 1$  indicates the degree of unidirectionality in the hopping with  $u = 0$  being the Hermitian limit of bidirectional hopping and  $u = 1$  being the limit of fully unidirectional hopping. The Hamiltonian is non-Hermitian for  $u > 0$ . With translational invariance and periodic boundary conditions, it is possible to Fourier transform the Hamiltonian as  $H^{(m,n)}(u) = \sum_k c_k^\dagger \mathcal{H}^{(m,n)}(k, u) c_k$  where  $c_k^\dagger = (c_{k,A1}^\dagger \dots c_{k,Am}^\dagger \ c_{k,B1}^\dagger \dots c_{k,Bn}^\dagger)$  and the Bloch Hamiltonian  $\mathcal{H}^{(m,n)}(k, u)$  is a  $p \times p$  matrix. For the rest of this section, we consider  $u = 1$ .

We consider a parent model which is a Hermitian tight-binding model on a bipartite lattice ( $p = 2$ ), with  $A$  and  $B$  sublattices and a  $2 \times 2$  Bloch Hamiltonian of the form

$$\mathcal{H}^{(1,1)}(k, 0) = \begin{pmatrix} 0 & h^*(k) \\ h(k) & 0 \end{pmatrix}. \quad (2)$$

This satisfies chiral symmetry as  $\sigma_z \mathcal{H}^{(1,1)}(k, 0) \sigma_z = -\mathcal{H}^{(1,1)}(k, 0)$  where  $\sigma_z$  is the diagonal Pauli spin matrix, and it has two energy bands  $\epsilon_j^{(1,1)}(k, 0) = (-1)^j |h(k)|$  for  $j = 1, 2$ .

A non-Hermitian model is formed from the parent by adding additional orbitals on either the  $A$  or the  $B$  site and introducing unidirectional hopping. For the example of the SSH model with  $p = 3$ , Fig. 1(b), the non-Hermitian model is formed by adding an additional orbital on site  $B$ , to give orbitals  $B1$  and  $B2$  on site  $B$ , with a new Bloch Hamiltonian in the  $A, B1, B2$  basis,

$$\mathcal{H}^{(1,2)}(k, 1) = \begin{pmatrix} 0 & 0 & h^*(k) \\ h(k) & 0 & 0 \\ 0 & \gamma & 0 \end{pmatrix}, \quad (3)$$

where  $\gamma > 0$  is the amplitude for unidirectional hopping from  $B1$  to  $B2$ . This Hamiltonian satisfies a complex generalization of chiral symmetry,  $Z \mathcal{H}^{(1,2)}(k, 1) Z^{-1} = \omega \mathcal{H}^{(1,2)}(k, 1)$ , where  $Z$  is a  $3 \times 3$  generalization of  $\sigma_z$ ,  $Z = \text{diag}(1, \omega, \omega^2)$  with  $\omega = \exp(2\pi i/3)$  [44–46]. There are three complex energy bands related to those of the parent model as  $\epsilon_j^{(1,2)}(k, 1) = \omega^j (\gamma |h(k)|^2)^{1/3}$  for  $j = 1, 2, 3$ , and the topology of the model is related to that of the parent as illustrated in Fig. 1(c) and (d).

In general, the Bloch Hamiltonian  $\mathcal{H}^{(m,n)}(k, 1)$  is a  $p \times$

$p$  matrix,  $p = m + n$ , with matrix elements given by

$$\begin{aligned} \mathcal{H}_{m+1,m}^{(m,n)}(k, 1) &= \left( \mathcal{H}_{1,m+n}^{(m,n)}(k, 1) \right)^* = h(k), \quad (4) \\ \mathcal{H}_{\ell+1,\ell}^{(m,n)}(k, 1) &= \gamma, \end{aligned}$$

for  $\ell = 1, 2, \dots, m-1$  and  $\ell = m+1, \dots, p-1$ . All other matrix elements are zero. This matrix is a generalized permutation matrix with only one non-zero entry in each row and each column. It has an element on the end of the first row,  $\mathcal{H}_{1,m+n}^{(m,n)}(k, 1) = h^*(k)$ , and all other non-zero matrix elements are along the lower diagonal. As a result, the Hamiltonian satisfies the complex generalization of chiral symmetry (1).

The Bloch Hamiltonian  $\mathcal{H}^{(m,n)}(k, 1)$  may be viewed as a  $p$ th root of the parent model squared  $(\mathcal{H}^{(1,1)}(k, 0))^2$ , generalizing the concept of square root Hamiltonians [46, 50, 64–72]. Chiral symmetry behaves as a unitary symmetry when applied to the Bloch Hamiltonian raised to the  $p$ th power,  $Z (\mathcal{H}^{(m,n)}(k, 1))^p Z^{-1} = (\mathcal{H}^{(m,n)}(k, 1))^p$ , block diagonalizing it into  $p$  separate blocks. Hence,  $(\mathcal{H}^{(m,n)}(k, 1))^p$  is diagonal [45],

$$\left( \mathcal{H}^{(m,n)}(k, 1) \right)^p = \gamma^{p-2} |h(k)|^2 \mathbb{I}_p, \quad (5)$$

where  $\mathbb{I}_p$  is the  $p \times p$  identity matrix. Thus,  $p$  complex energy bands  $\epsilon_j^{(m,n)}(k, 1)$ ,  $j = 1, 2, \dots, p$ , of  $\mathcal{H}^{(m,n)}(k, 1)$  are given by the distinct solutions of

$$\left( \epsilon_j^{(m,n)}(k, 1) \right)^p = \gamma^{p-2} |h(k)|^2. \quad (6)$$

The Bloch Hamiltonian  $\mathcal{H}^{(n,n)}(k, 1)$  is an  $n$ th root of the parent Hamiltonian  $\mathcal{H}^{(1,1)}(k, 0)$ . This means that  $(\mathcal{H}^{(n,n)}(k, 1))^n$  may be written as being block diagonal, using a unitary transformation to re-order the basis, with  $n$  separate blocks, each of which is a  $2 \times 2$  matrix,  $\gamma^{n-1} \mathcal{H}^{(1,1)}(k, 0)$ .

### B. Exceptional points

The Bloch Hamiltonian  $\mathcal{H}^{(m,n)}(k, 1)$  has an exceptional point at  $h(k) = 0$  [13, 15–17, 27–43, 46]. In particular, it has defective eigenvalues whereby their algebraic multiplicity, as defined by the roots of the characteristic polynomial, is greater than their geometric multiplicity, the number of associated linearly-independent eigenvectors. For  $u = 1$  and  $h(k) = 0$ , all eigenvalues of  $\mathcal{H}^{(m,n)}(k, 1)$  are at zero energy with an algebraic multiplicity of  $p$  and a geometric multiplicity of two with partial degeneracies [41, 43] ( $l_1, l_2$ ) =  $(m, n)$  associated with the  $A$  and  $B$  sites, respectively. For the SSH model,  $h(k) \neq 0$  for the bulk in the gapped phases, but the defective eigenvalues may be manifested at edges, as described in Sec. III B, and on domain walls, Sec. III E.

### C. The non-Hermitian SSH model

The Hermitian SSH model has the form of  $\mathcal{H}^{(1,1)}(k, 0)$ , Eq. (2), with  $h(k) = t + Je^{ika}$  where  $t \geq 0$  describes intracell hopping,  $J \geq 0$  is intercell hopping, and  $a$  is the lattice constant. The lattice in position space is shown in Fig. 1(a). As well as chiral symmetry (1) with  $Z = \sigma_z$  (the diagonal Pauli spin matrix) and  $\omega = -1$ , the model has time-reversal symmetry  $(\mathcal{H}^{(1,1)}(k, 0))^* = \mathcal{H}^{(1,1)}(-k, 0)$  and charge-conjugation symmetry  $\sigma_z (\mathcal{H}^{(1,1)}(k, 0))^* \sigma_z = -\mathcal{H}^{(1,1)}(-k, 0)$ . It has two energy bands given by Eq. (6),

$$\epsilon_j^{(1,1)}(k) = (-1)^j \sqrt{t^2 + J^2 + 2tJ \cos(ka)}. \quad (7)$$

The non-Hermitian model (4) has time-reversal symmetry  $(\mathcal{H}^{(m,n)}(k, 1))^* = \mathcal{H}^{(m,n)}(-k, 1)$ , generalized chiral symmetry (1) and generalized charge-conjugation symmetry  $Z (\mathcal{H}^{(m,n)}(k, 1))^* Z^{-1} = \omega \mathcal{H}^{(m,n)}(-k, 1)$  where  $\omega = \exp(2\pi i/p)$ . There are  $p$  complex energy bands  $\epsilon_j^{(m,n)}(k)$ ,  $j = 1, 2, \dots, p$ , given by

$$(\epsilon_j^{(m,n)}(k))^p = \gamma^{p-2} (t^2 + J^2 + 2tJ \cos(ka)), \quad (8)$$

which are gapless at  $k = \pi/a$  for  $t = J$ , as for the SSH model.

### D. Relation to free parafermions

When the SSH model is the parent model, the single-particle energy levels are the same as those of free parafermions in Baxter's clock model [44, 73, 74]. This connection may be understood by considering the form of the Hamiltonian  $H^{(1,p-1)}(u=1)$  in position space,

$$H^{(1,p-1)}(u=1) = \sum_{j,m=1}^{pL} c_j^\dagger \mathcal{H}_{j,m}^{(1,p-1)} c_m, \quad (9)$$

where  $c_j^\dagger$  and  $c_j$  are creation and annihilation operators for spinless fermions on site  $j$ ,  $p$  is the number of orbitals per unit cell,  $L$  is the number of unit cells, and  $\mathcal{H}^{(1,p-1)}$  is a  $pL \times pL$  matrix. Intercell terms are given by

$$\begin{aligned} \mathcal{H}_{(\ell-1)p+1,\ell p}^{(1,p-1)} &= \mathcal{H}_{(\ell-1)p+2,(\ell-1)p+1}^{(1,p-1)} = t, \\ \mathcal{H}_{(\ell-1)p+m+2,(\ell-1)p+m+1}^{(1,p-1)} &= \gamma, \end{aligned}$$

for  $\ell = 1, 2, \dots, L$  and  $m = 1, 2, \dots, p-2$ , and intracell terms are given by

$$\mathcal{H}_{(\ell-1)p+2,\ell p+1}^{(1,p-1)} = \mathcal{H}_{\ell p+1,\ell p}^{(1,p-1)} = J,$$

for  $\ell = 1, 2, \dots, (L-1)$ , where  $t \geq 0$ ,  $J \geq 0$  and  $\gamma > 0$  are real. All other matrix elements are zero, and we assume open boundary conditions.

As examples, the Hermitian SSH model [1–3], Fig. 1(a), corresponds to  $p = 2$ ,

$$\mathcal{H}^{(1,1)} = \begin{pmatrix} 0 & t & 0 & 0 & 0 & \dots & 0 & 0 & 0 \\ t & 0 & J & 0 & 0 & \dots & 0 & 0 & 0 \\ 0 & J & 0 & t & 0 & \dots & 0 & 0 & 0 \\ 0 & 0 & t & 0 & J & \dots & 0 & 0 & 0 \\ 0 & 0 & 0 & J & 0 & \dots & 0 & 0 & 0 \\ \vdots & \vdots & \vdots & \vdots & \vdots & \ddots & \vdots & \vdots & \vdots \\ 0 & 0 & 0 & 0 & 0 & \dots & 0 & J & 0 \\ 0 & 0 & 0 & 0 & 0 & \dots & J & 0 & t \\ 0 & 0 & 0 & 0 & 0 & \dots & 0 & t & 0 \end{pmatrix}. \quad (10)$$

For  $p = 3$ ,  $\mathcal{H}^{(1,2)}$ , Fig. 1(b), is given by

$$\mathcal{H}^{(1,2)} = \begin{pmatrix} 0 & 0 & t & 0 & 0 & 0 & 0 & \dots & 0 & 0 & 0 & 0 \\ t & 0 & 0 & J & 0 & 0 & 0 & \dots & 0 & 0 & 0 & 0 \\ 0 & \gamma & 0 & 0 & 0 & 0 & 0 & \dots & 0 & 0 & 0 & 0 \\ 0 & 0 & J & 0 & 0 & t & 0 & \dots & 0 & 0 & 0 & 0 \\ 0 & 0 & 0 & t & 0 & 0 & J & \dots & 0 & 0 & 0 & 0 \\ 0 & 0 & 0 & 0 & \gamma & 0 & 0 & \dots & 0 & 0 & 0 & 0 \\ 0 & 0 & 0 & 0 & 0 & J & 0 & \dots & 0 & 0 & 0 & 0 \\ \vdots & \ddots & \vdots & \vdots & \vdots & \vdots \\ 0 & 0 & 0 & 0 & 0 & 0 & 0 & \dots & J & 0 & 0 & t \\ 0 & 0 & 0 & 0 & 0 & 0 & 0 & \dots & 0 & t & 0 & 0 \\ 0 & 0 & 0 & 0 & 0 & 0 & 0 & \dots & 0 & 0 & \gamma & 0 \end{pmatrix}. \quad (11)$$

The matrices  $\mathcal{H}^{(1,p-1)}$  are the same as the matrices in the construction [44] of generalized raising and lowering operators for  $p$ -state parafermions (denoted  $\mathcal{M}_n$  in [44]), except for re-scaling of the hopping parameters. Hence, they have the same single-particle energy levels as free parafermions. In particular, for a system with  $L$  unit cells, the SSH model  $\mathcal{H}^{(1,1)}$  has  $L$  positive eigenvalues, denoted  $\epsilon_j^{\text{SSH}}$ , and  $\mathcal{H}^{(m,n)}$  has  $pL$  eigenvalues  $\epsilon_j^{(p)}$  given by

$$(\epsilon_j^{(p)})^p = \gamma^{p-2} (\epsilon_j^{\text{SSH}})^2, \quad (12)$$

where  $j = 1, 2, \dots, L$  and  $p = m + n$ .

## III. PARTIAL UNIDIRECTIONAL HOPPING

### A. Symmetries

We now consider systems with partial unidirectional hopping by considering the Hamiltonian

$$\mathcal{H}^{(m,n)}(k, u) = \mathcal{H}^{(m,n)}(k, 1) + (1-u)(\mathcal{H}^{(m,n)}(k, 1))^\dagger, \quad (13)$$

where  $\mathcal{H}^{(m,n)}(k, 1)$  is the fully unidirectional Bloch Hamiltonian defined in Eq. (4) and the degree of directionality  $0 \leq u \leq 1$ . Hamiltonian  $\mathcal{H}^{(m,n)}(k, u)$  is Hermitian for  $u = 0$  and non-Hermitian otherwise.

We begin by describing the symmetries of  $\mathcal{H}^{(m,n)}(k, u)$  using the definitions of the symmetry classification for non-Hermitian Hamiltonians [85, 86]. Throughout this paper, we consider only real tight-binding parameters, so  $\mathcal{H}^{(m,n)}(k, u)$  satisfies time-reversal symmetry,

$$(\mathcal{H}^{(m,n)}(k, u))^* = \mathcal{H}^{(m,n)}(-k, u), \quad (14)$$

for all  $u$  values. This dictates that the energy spectrum is either real or comes with complex-conjugate pairs [85] (it has reflection symmetry in the real energy axis). For fully unidirectional hopping,  $u = 1$ , the Hamiltonian also satisfies complex chiral symmetry (1) and this guarantees that the spectrum has the form (6) given by the  $p$ th roots of unity and the parent model. The combination of time-reversal symmetry and chiral symmetry (1) gives a generalized particle-hole symmetry  $Z(\mathcal{H}^{(m,n)}(k, 1))^* Z^{-1} = \omega \mathcal{H}^{(m,n)}(-k, 1)$ .

For partial unidirectional hopping,  $0 < u < 1$ , the symmetries depend on whether the number of orbitals per cell  $p = m + n$  is even or odd. For odd  $p$ , the Hamiltonian is pseudo-Hermitian  $\eta(\mathcal{H}^{(m,n)}(k, u))^\dagger \eta^{-1} = \mathcal{H}^{(m,n)}(k, u)$  where  $\eta$  is unitary and Hermitian [86, 87]. Combined with time-reversal symmetry, this gives a variant time-reversal symmetry,  $\mathcal{C}_+(\mathcal{H}^{(m,n)}(k, u))^T \mathcal{C}_+^{-1} = \mathcal{H}^{(m,n)}(-k, u)$  where  $\mathcal{C}_+ \mathcal{C}_+^* = +1$  [86]. For even  $p$ , the Hamiltonian obeys sublattice symmetry  $S \mathcal{H}^{(m,n)}(k, u) S^{-1} = -\mathcal{H}^{(m,n)}(k, u)$  where  $S^2 = 1$  [86]. Combined with time-reversal symmetry, this gives a variant particle-hole symmetry,  $\mathcal{T}_-(\mathcal{H}^{(m,n)}(k, u))^* \mathcal{T}_-^{-1} = -\mathcal{H}^{(m,n)}(-k, u)$  where  $\mathcal{T}_- \mathcal{T}_-^* = +1$  [86]. This dictates that the energy spectrum for even  $p$  is either purely imaginary or comes with  $(\epsilon, -\epsilon^*)$  pairs [85] (it has reflection symmetry in the imaginary energy axis).

For bidirectional hopping,  $\mathcal{H}^{(m,n)}(k, 0)$  is an Hermitian Hamiltonian. It can be block diagonalized into even and odd parity blocks with respect to inversion of the orbitals within the unit cell. Partially unidirectional hopping  $u > 0$  breaks the inversion symmetry and mixes the even and odd blocks, and the real energy spectrum evolves into a complex one as the degree of unidirectionality  $u$  increases. This process is determined by the topology of the parent model and by the number of orbitals per unit cell,  $p = m + n$ . Below, we describe this process in detail for  $p = 3$  and  $p = 4$  with the example of the SSH model.

## B. $H^{(1,2)}$

There is one model with  $p = 3$ ,  $H^{(1,2)}$ , with one orbital on the  $A$  site and two on the  $B$  site, Fig. 1(b). The Bloch Hamiltonian  $\mathcal{H}^{(1,2)}(k, 1)$  written in the  $A$ ,  $B1$ ,  $B2$  basis is given by Eq. (3). In the bidirectional limit, there is a symmetry related to swapping the  $B1$  and  $B2$  orbitals. Hence, we write the Hamiltonian  $\mathcal{H}^{(1,2)}(k, u)$  in a basis of even and odd parity states,  $A$ ,  $(B1 + B2)/\sqrt{2}$ ,  $(B1 -$

$B2)/\sqrt{2}$ , as

$$\tilde{\mathcal{H}}^{(1,2)}(k, u) = \begin{pmatrix} 0 & \sqrt{2}\tilde{h}^*(k) & -\sqrt{2}\tilde{u}\tilde{h}^*(k) \\ \sqrt{2}\tilde{h}(k) & \tilde{\gamma} & \tilde{u}\tilde{\gamma} \\ \sqrt{2}\tilde{u}\tilde{h}(k) & -\tilde{u}\tilde{\gamma} & -\tilde{\gamma} \end{pmatrix}, \quad (15)$$

where

$$\tilde{h}(k) = (1 - u/2)h(k), \quad (16)$$

$$\tilde{\gamma} = (1 - u/2)\gamma, \quad (17)$$

$$\tilde{u} = u/(2 - u). \quad (18)$$

This explicitly illustrates that the unidirectional hopping  $u$  breaks the inversion symmetry and mixes the even and odd blocks.

The odd state gives a flat band [66, 68, 88–91], and the even  $2 \times 2$  block takes a form similar to the parent model, but with different onsite energies (this is the Rice-Mele model [92] if the parent Hamiltonian is the SSH model). The energy eigenvalues of the even and odd blocks on their own are

$$E_{1,2}(k) = \frac{\tilde{\gamma}}{2} \pm \sqrt{\frac{\tilde{\gamma}^2}{4} + 2|\tilde{h}|^2}, \quad (19)$$

$$E_3 = -\tilde{\gamma}. \quad (20)$$

Now we write the Hamiltonian in the eigenbasis of these states,

$$\bar{\mathcal{H}}^{(1,2)}(k, u) = \begin{pmatrix} E_1 & 0 & -\tilde{u}a_1 \\ 0 & E_2 & -\tilde{u}a_2 \\ \tilde{u}a_1 & \tilde{u}a_2 & E_3 \end{pmatrix}, \quad (21)$$

where

$$a_{1,2} = \frac{2 \left( |\tilde{h}|^2 - \tilde{\gamma}E_{1,2}/2 \right)}{\sqrt{E_{1,2}^2 + 2|\tilde{h}|^2}}. \quad (22)$$

Depending on the particular form of  $h(k)$ , energies  $E_2$  and  $E_3$  are degenerate or nearly degenerate for some  $k$  values. For small  $u$ , we describe the mixing of these degenerate states using a  $2 \times 2$  effective Hamiltonian,

$$\mathcal{H}_{\text{eff}}^{(1,2)}(k, u) = \begin{pmatrix} E_2 & -\tilde{u}a_2 \\ \tilde{u}a_2 & -\tilde{\gamma} \end{pmatrix}, \quad (23)$$

which has energies

$$\epsilon_{\pm}(k) = \frac{E_2 - \tilde{\gamma}}{2} \pm \sqrt{\frac{(E_2 + \tilde{\gamma})^2}{4} - \tilde{u}^2 a_2^2}. \quad (24)$$

As  $u$  increases, the band energies  $\epsilon_{\pm}(k)$  evolve from being purely real to being complex. Since  $|h(k)|$  varies across the band, the evolution is done via the formation of a circular band structure, centered on the real axis.

For the SSH model,  $h(k) = t + J e^{ika}$ . Across the first Brillouin zone, the maximum value of  $|h(k)|$  is  $|t + J|$

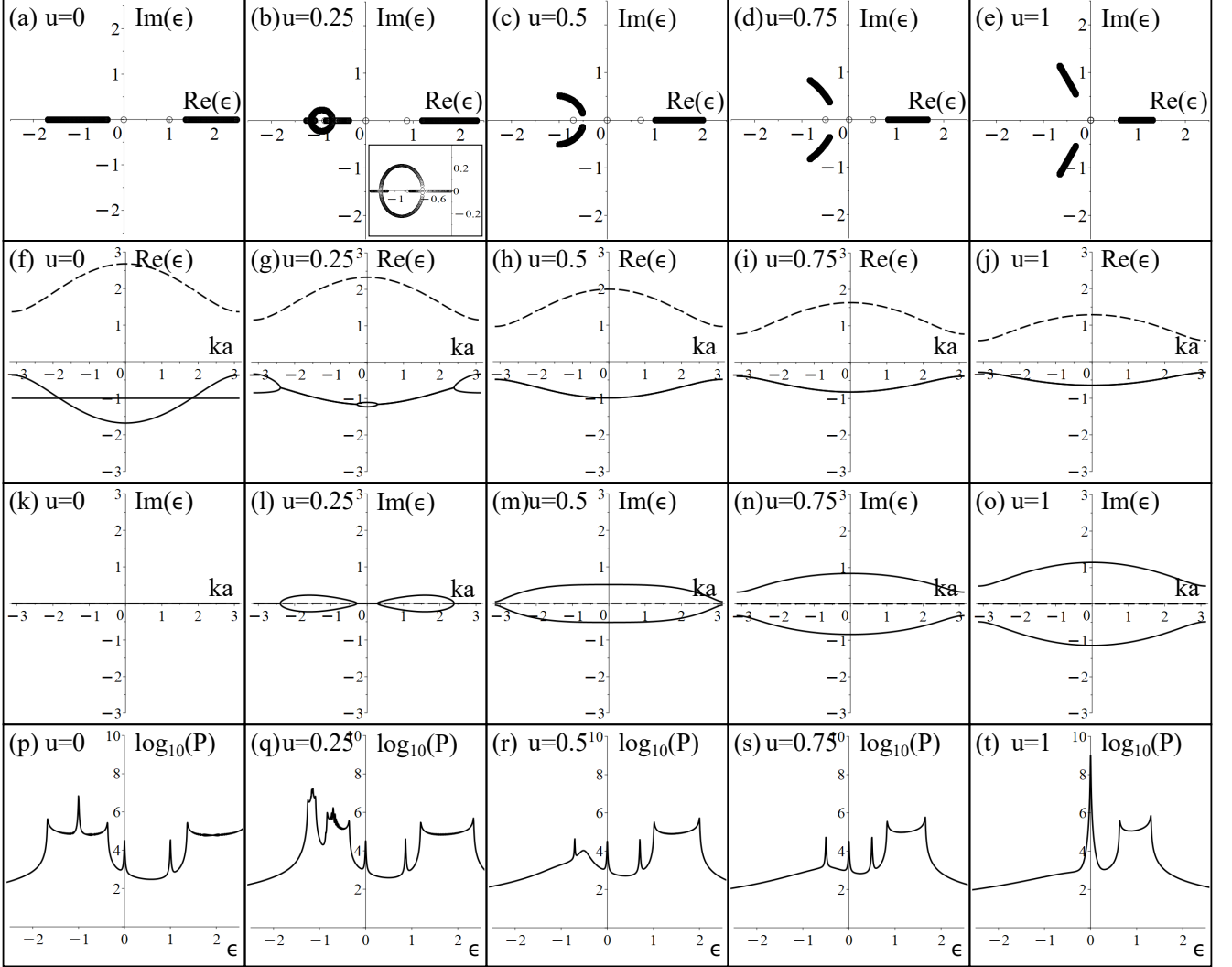


FIG. 2. Complex energy spectra for  $p = 3$  orbitals, model  $H^{(1,2)}$ , as a function of the degree of unidirectionality  $u$  when the SSH model is the parent model. The top row shows energy eigenvalues (circles) determined numerically in position space by diagonalizing  $\mathcal{H}^{(1,2)}(u) = \mathcal{H}^{(1,2)}(1) + (1-u)(\mathcal{H}^{(1,2)}(1))^\dagger$  where  $\mathcal{H}^{(1,2)}(1)$  is given in Eq. (11), using open boundary conditions and  $L = 200$  unit cells. The inset in (b) shows a close up of the region where the eigenvalues form a circular shape. For all  $u$  values, there are three edge states with energies on the real axis (isolated circles, except one is obscured by other energies in (a) and (b)), and they are threefold degenerate at zero energy for  $u = 1$  in (e). The second row shows the real part of the energy bands and the third row shows their imaginary part, plotted for  $-\pi \leq ka \leq \pi$  and obtained by diagonalizing the Bloch Hamiltonian (21). Dashed lines show the band which is always real, and solid lines show the two bands which are partly real and partly imaginary. When the imaginary parts of the latter (solid lines) are non-zero, their real parts are superimposed on each other and appear as a single line in the plots. The bottom row shows the response power  $P(\epsilon)$  (25) as a function of real energy  $\epsilon$  determined in position space using open boundary conditions and  $L = 200$  unit cells. To smooth these plots, we add a small imaginary energy as  $\epsilon + i\delta$  where  $\delta = 0.005$ . In all plots, parameter values are  $t = 0.5$  and  $J = \gamma = 1.0$ .

and the minimum value is  $|t - J|$ . The evolution of the complex energy spectra as a function of the degree of unidirectionality  $u$  is shown in Fig. 2 (top row). Energy eigenvalues are determined numerically in position space with open boundary conditions by diagonalizing  $\mathcal{H}^{(1,2)}(u) = \mathcal{H}^{(1,2)}(1) + (1-u)(\mathcal{H}^{(1,2)}(1))^\dagger$  where  $\mathcal{H}^{(1,2)}(1)$  is given in Eq. (11). Parameter values are  $t = 0.5$ ,  $J = \gamma = 1.0$ , and there are  $L = 200$  unit cells. In Fig. 2, the second row shows the real part of the energy bands

and the third row shows their imaginary part, plotted for  $-\pi \leq ka \leq \pi$  and obtained by diagonalizing the Bloch Hamiltonian (21).

For  $u = 0$ , Fig. 2(a), the even parity blocks give two real bands equivalent to the Rice-Mele model [92] with a band gap centered on energy  $\gamma/2$  (19). In addition, the odd parity states give a flat band at energy  $-\gamma$  (20). For  $u = 0.25$ , Fig. 2(b), the two bands with  $\text{Re}(\epsilon) < 0$  have some purely real energies and some complex ones forming

a circular structure according to Eq. (24). For  $u = 0.5$ , Fig. 2(c), these two bands contain no purely real energy values, and they continue to evolve until  $u = 1$ , Fig. 2(e), where they are described by Eq. (8).

With  $t < J$ , the parent SSH model is in the topologically nontrivial phase. For all  $u$  values, there are edge states with real energies, shown in Fig. 2 (top row). Their energies may be estimated by considering the trimer limit  $t = 0$ , Fig. 1(d), in which there are three edge states: one on the left side has energy  $\epsilon = 0$  and two on the right side have energies  $\epsilon = \pm\gamma\sqrt{1-u}$ . These estimates are a good approximation for  $J > t > 0$  beyond the trimer limit in a large enough system, and they are in excellent agreement with the numerical data in Fig. 2.

In general, the edge states give defective eigenvalues when  $u = 1$ ,  $t = 0$ . They are at zero energy with an algebraic multiplicity of  $p$  and a geometric multiplicity of two with partial degeneracies [41, 43]  $(l_1, l_2) = (m, n)$ , partitioned according to the left and right ends of the system. The defective eigenvalues produce a characteristic resonant response determined by the largest partial degeneracy  $\ell_m = \max(m, n)$  [41, 43]. With the Green's function  $G(\epsilon) = (\epsilon\mathbb{I} - \mathcal{H}^{(m,n)})^{-1}$ , the spectrally resolved response power [41–43] is

$$P(\epsilon) = \text{tr}\{[G(\epsilon)]^\dagger G(\epsilon)\}. \quad (25)$$

For the edge states, we find that

$$P(\epsilon) \sim \frac{\gamma^{2\ell_m-2}}{|\epsilon|^{2\ell_m}}; \quad \ell_m = \max(m, n), \quad (26)$$

for  $u = 1$ ,  $t = 0$ , and energy  $\epsilon$  near zero, in agreement with Refs. [41, 43]. The power (25) as a function of the degree of unidirectionality  $u$  is plotted for  $H^{(1,2)}$  in Fig. 2 (bottom row) for  $J > t > 0$ , determined numerically in position space with open boundary conditions. There are plateaus at the location of the bands (on the real energy axis) and distinctive peaks corresponding to the edge states, with the most prominent peak appearing at zero energy for  $u = 1$ . Similar peaks will appear due to states localized on domain walls, as described in Sec. III E.

### C. $H^{(1,3)}$

There are two models with  $p = 4$ ,  $H^{(1,3)}$  and  $H^{(2,2)}$ :  $H^{(1,3)}$  has one orbital on the  $A$  site and three on the  $B$  site, Fig. 3(a). In the bidirectional limit, there is a symmetry related to swapping the  $B1$  and  $B3$  orbitals. Hence, we write the Hamiltonian  $\mathcal{H}^{(1,3)}(k, u)$  in a basis of even and odd parity states,  $A$ ,  $(B1 + B3)/\sqrt{2}$ ,  $B2$ ,  $(B1 - B3)/\sqrt{2}$ , as

$$\tilde{\mathcal{H}}^{(1,3)}(k, u) = \sqrt{2} \begin{pmatrix} 0 & \tilde{h}^*(k) & 0 & -\tilde{u}\tilde{h}^*(k) \\ \tilde{h}(k) & 0 & \tilde{\gamma} & 0 \\ 0 & \tilde{\gamma} & 0 & \tilde{u}\tilde{\gamma} \\ \tilde{u}\tilde{h}(k) & 0 & -\tilde{u}\tilde{\gamma} & 0 \end{pmatrix}, \quad (27)$$

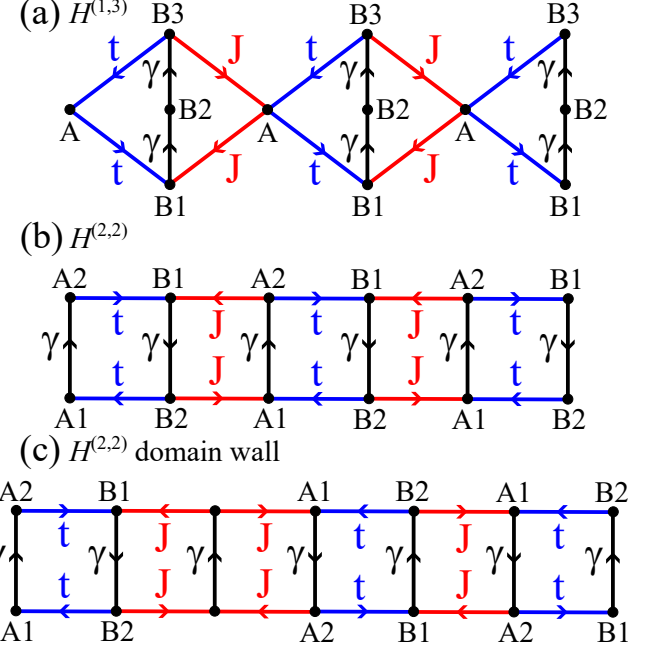


FIG. 3. Non-Hermitian Hamiltonians formed from the parent SSH model with  $p = 4$  orbitals per unit cell. (a) Model  $H^{(1,3)}$  with three orbitals  $B1$ ,  $B2$ ,  $B3$  connected by unidirectional hopping  $\gamma > 0$  as indicated by the arrows, with unidirectional hopping from  $A$  to  $B1$  and from  $B3$  to  $A$ . (b) Model  $H^{(2,2)}$  with two orbitals  $A1$ ,  $A2$  and two orbitals  $B1$ ,  $B2$  connected by unidirectional hopping  $\gamma > 0$ , with unidirectional hopping from  $A2$  to  $B1$  and from  $B2$  to  $A1$ . (c) Model  $H^{(2,2)}$  with a domain wall hosting localized states.

using the definitions in Eqs. (16)-(18). The even  $3 \times 3$  block has two dispersive bands plus a flat band at zero energy. The odd state also gives a flat band at zero energy. The energy eigenvalues of the even and odd blocks on their own are

$$E_{1,2}(k) = \pm \sqrt{2(\tilde{\gamma}^2 + |\tilde{h}|^2)}, \quad (28)$$

$$E_3 = E_4 = 0, \quad (29)$$

and the Hamiltonian in the eigenbasis of these states is

$$\bar{\mathcal{H}}^{(1,3)}(k, u) = \begin{pmatrix} E_1 & 0 & 0 & \tilde{u}b_1 \\ 0 & E_2 & 0 & \tilde{u}b_1 \\ 0 & 0 & 0 & \tilde{u}b_2^* \\ -\tilde{u}b_1 & -\tilde{u}b_1 & -\tilde{u}b_2 & 0 \end{pmatrix}, \quad (30)$$

where

$$b_1 = \frac{(\tilde{\gamma}^2 - |\tilde{h}|^2)}{\sqrt{\tilde{\gamma}^2 + |\tilde{h}|^2}}, \quad b_2 = \frac{2\sqrt{2}\tilde{\gamma}\tilde{h}}{\sqrt{\tilde{\gamma}^2 + |\tilde{h}|^2}}. \quad (31)$$

For small  $u$ , we consider a  $2 \times 2$  effective Hamiltonian describing mixing of the two zero-energy flat bands,

$$\mathcal{H}_{\text{eff}}^{(1,3)}(k, u) = \begin{pmatrix} 0 & \tilde{u}b_2^* \\ -\tilde{u}b_2 & 0 \end{pmatrix}, \quad (32)$$

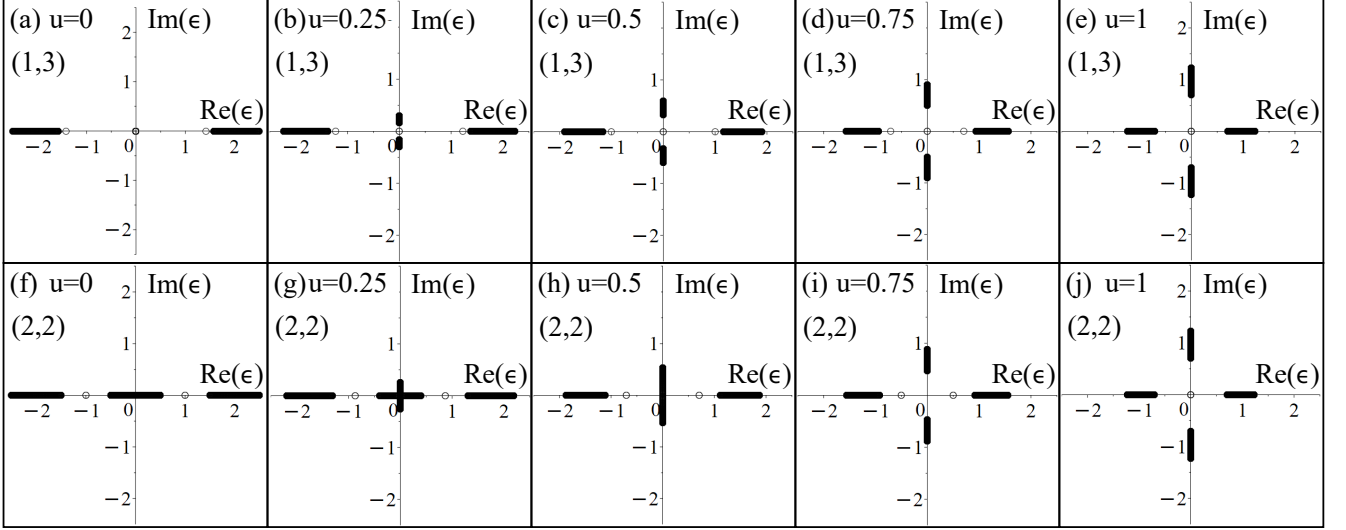


FIG. 4. Complex energy spectra for  $p = 4$  orbitals, as a function of the degree of unidirectionality  $u$  when the SSH model is the parent model. The top row shows model  $H^{(1,3)}$ , the bottom row  $H^{(2,2)}$ . Energy eigenvalues (circles) are determined numerically in position space with open boundary conditions by diagonalizing the Hamiltonian. Parameter values are  $t = 0.5$ ,  $J = \gamma = 1.0$ , and there are  $L = 200$  unit cells. For all  $u$  values, there are four edge states with energies on the real axis (isolated circles). For  $H^{(1,3)}$  (top row), two are degenerate at zero energy, the other two are at non-zero energy for  $u < 1$ . For  $H^{(2,2)}$  (bottom row), the edge states are twofold degenerate for all  $u < 1$ . For  $u = 1$ , the edge states are fourfold degenerate at zero energy in (e) and (j).

which has energies

$$\epsilon_{\pm}(k) = \pm \frac{2\sqrt{2}i\tilde{u}\tilde{\gamma}|\tilde{h}(k)|}{\sqrt{\tilde{\gamma}^2 + |\tilde{h}(k)|^2}}. \quad (33)$$

Hence these two bands are purely imaginary for  $u > 0$  (and  $|\tilde{h}(k)| \neq 0$ ).

The evolution of the complex energy spectra as a function of the degree of unidirectionality  $u$  is shown in Fig. 4 (top row). Energy eigenvalues are determined numerically in position space with open boundary conditions. Parameter values are  $t = 0.5$ ,  $J = \gamma = 1.0$ , and there are  $L = 200$  unit cells. For all  $u$ , all energies lie on either the real or the imaginary axes. For  $u = 0$ , Fig. 4(a), energies are given by Eqs. (28) and (29) with two degenerate flat bands at zero energy. For  $u > 0$ , Fig. 4(b), these two bands become purely imaginary and dispersive, in accordance with Eq. (33). They remain on the imaginary axis for all subsequent  $u$ , and, at  $u = 1$ , Fig. 4(e), where they are described by Eq. (8).

With  $t < J$ , there are four edge states with real energies for all  $u$  values, shown in Fig. 4 (top row). Their energies may be estimated by considering the limit  $t = 0$  in Fig. 3(a). One edge state on the left side has energy  $\epsilon = 0$  and three on the right side have energies  $\epsilon = 0$  and  $\epsilon = \pm\gamma\sqrt{2(1-u)}$ . These estimates are a good approximation for  $J > t > 0$  beyond the  $t = 0$  limit in a large enough system, and they are in excellent agreement with the numerical data in Fig. 4 (top row).

#### D. $H^{(2,2)}$

The non-Hermitian model  $H^{(2,2)}$  has two orbitals on the  $A$  site and two on the  $B$  site, Fig. 3(b). Unlike  $H^{(1,2)}$  and  $H^{(1,3)}$ , there is parity related to inverting the whole system (e.g. swapping  $A1$  on the left edge with  $B1$  on the right edge in Fig. 3(b)); the parent (SSH) model has an analogous symmetry. In the bidirectional limit,  $H^{(2,2)}$  corresponds to two coupled SSH chains [93–97], and, as with the other models, there is symmetry related to swapping orbitals within the unit cell ( $A1$  and  $A2$ , and  $B1$  and  $B2$ ). We write the Hamiltonian  $\tilde{\mathcal{H}}^{(2,2)}(k, u)$  in a basis of even and odd parity states,  $(A1+A2)/\sqrt{2}$ ,  $(B1+B2)/\sqrt{2}$ ,  $(A1-A2)/\sqrt{2}$ ,  $(B1-B2)/\sqrt{2}$ , as

$$\tilde{\mathcal{H}}^{(2,2)}(k, u) = \begin{pmatrix} \tilde{\gamma} & \tilde{h}^*(k) & \tilde{u}\tilde{\gamma} & -\tilde{u}\tilde{h}^*(k) \\ \tilde{h}(k) & \tilde{\gamma} & -\tilde{u}\tilde{h}(k) & \tilde{u}\tilde{\gamma} \\ -\tilde{u}\tilde{\gamma} & \tilde{u}\tilde{h}^*(k) & -\tilde{\gamma} & -\tilde{h}^*(k) \\ \tilde{u}\tilde{h}(k) & -\tilde{u}\tilde{\gamma} & -\tilde{h}(k) & -\tilde{\gamma} \end{pmatrix}, \quad (34)$$

using the definitions in Eqs. (16)-(18). The even  $2 \times 2$  block takes the form of the parent model centered on energy  $\tilde{\gamma}$  and the odd  $2 \times 2$  block takes the form of the parent model centered on energy  $-\tilde{\gamma}$ . The energy eigenvalues of the even and odd blocks on their own are

$$E_1(k) = \tilde{\gamma} + |\tilde{h}|; \quad E_2(k) = \tilde{\gamma} - |\tilde{h}| \quad (35)$$

$$E_3(k) = -\tilde{\gamma} + |\tilde{h}|; \quad E_4(k) = -\tilde{\gamma} - |\tilde{h}|, \quad (36)$$

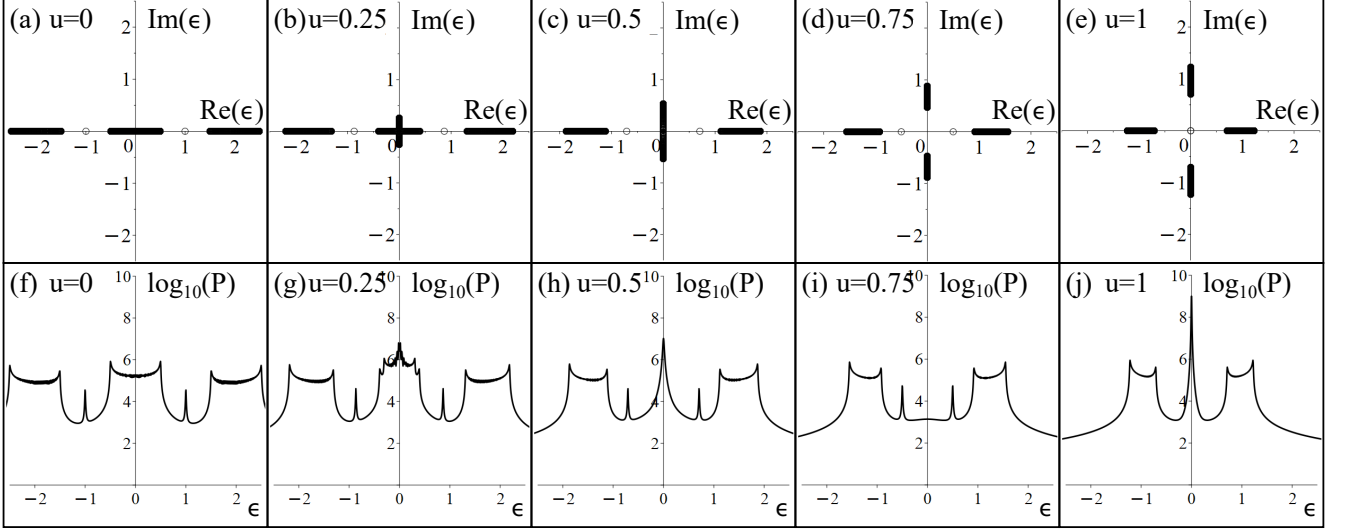


FIG. 5. Complex energy spectra (top row) and the response power  $P(\epsilon)$  (bottom row) with a domain wall in  $H^{(2,2)}$  when the SSH model is the parent model. All data is determined numerically in position space with open boundary conditions by diagonalizing the Hamiltonian. Parameter values are  $t = \gamma = 1.0$ ,  $J = 0.5$ , and there are 802 orbitals. We consider strong  $t$  bonds at the edges and a domain wall at the centre of the system. For the energy spectra (top row), states localized on the domain wall are isolated circles on the real energy axis, and they are twofold degenerate at zero energy for  $u = 1$ . The bottom row shows the response power  $P(\epsilon)$  (25) as a function of real energy  $\epsilon$  where we add a small imaginary energy as  $\epsilon + i\delta$  with  $\delta = 0.005$ .

and the Hamiltonian in the eigenbasis of these states may be written in a block diagonal form as

$$\tilde{\mathcal{H}}^{(2,2)}(k, u) = \begin{pmatrix} E_1 & \tilde{u}E_2 & 0 & 0 \\ -\tilde{u}E_2 & E_4 & 0 & 0 \\ 0 & 0 & E_2 & \tilde{u}E_1 \\ 0 & 0 & -\tilde{u}E_1 & E_3 \end{pmatrix}. \quad (37)$$

with energies

$$\epsilon_{r,\pm}(k) = \pm\sqrt{(\tilde{\gamma} + |\tilde{h}|)^2 - \tilde{u}^2(\tilde{\gamma} - |\tilde{h}|)^2}, \quad (38)$$

$$\epsilon_{i,\pm}(k) = \pm\sqrt{(\tilde{\gamma} - |\tilde{h}|)^2 - \tilde{u}^2(\tilde{\gamma} + |\tilde{h}|)^2}. \quad (39)$$

In terms of the original parameters, Eqs. (16)-(18),

$$\epsilon_{r,\pm}(k) = \pm\sqrt{(\gamma + [1-u]|h|)([1-u]\gamma + |h|)}, \quad (40)$$

$$\epsilon_{i,\pm}(k) = \pm\sqrt{(\gamma - [1-u]|h|)([1-u]\gamma - |h|)}. \quad (41)$$

Thus, there are two bands with real energies  $\epsilon_{r,\pm}(k)$  and two bands  $\epsilon_{i,\pm}(k)$  with energies that evolve from being purely real to being purely imaginary as  $u$  increases. For  $|h(k)| < \gamma$ , these bands are imaginary for  $|h(k)| > (1-u)\gamma$ .

The evolution of the complex energy spectra as a function of the degree of unidirectionality  $u$  is shown in Fig. 4 (bottom row). Energy eigenvalues are determined numerically in position space with open boundary conditions. Parameter values are  $t = 0.5$ ,  $J = \gamma = 1.0$ , and there are  $L = 200$  unit cells. For all  $u$ , all energies lie

on either the real or the imaginary axes. For  $u = 0$ , Fig. 4(f), the energies are those of two parent (SSH) models centered on  $\gamma$  and  $-\gamma$  as in Eqs. (35) and (36). For  $u > 0$ , Fig. 4(g), two bands become partly real and partly imaginary, Eq. (41). For large enough  $u$ , Fig. 4(h), they become wholly imaginary and, at  $u = 1$ , Fig. 4(j), they are described by Eq. (8).

With  $t < J$ , there are four edge states with real energies for all  $u$  values, shown in Fig. 4 (bottom row). Their energies may be estimated by considering the limit  $t = 0$  in Fig. 3(b). Two edge states on the left side have energies  $\epsilon = \pm\gamma\sqrt{(1-u)}$  and they are degenerate with two on the right side,  $\epsilon = \pm\gamma\sqrt{(1-u)}$ . These estimates are a good approximation for  $J > t > 0$  beyond the  $t = 0$  limit in a large enough system, and they are in excellent agreement with the numerical data in Fig. 4 (bottom row).

The Bloch Hamiltonian  $\mathcal{H}^{(n,n)}(k, 1)$  is an  $n$ th root of the parent Hamiltonian  $\mathcal{H}^{(1,1)}(k, 0)$ . With Eq. (34),  $(\tilde{\mathcal{H}}^{(2,2)}(k, u))^2$  is block diagonal, consisting of two  $2 \times 2$  blocks, each of which is

$$H_{\text{sq}}(u) = \begin{pmatrix} (1-u)(\gamma^2 + |h|^2) & (u^2 - 2u + 2)\gamma h^* \\ (u^2 - 2u + 2)\gamma h & (1-u)(\gamma^2 + |h|^2) \end{pmatrix}. \quad (42)$$

This has the parent model on the off-diagonal with an additional dispersing term on the diagonal, and, for  $u = 1$ , the diagonal term is zero.

### E. Localized states and exceptional points on solitons

When the SSH model is the parent model, there are edge states with real energies for  $t < J$  and, for  $u = 1$ ,  $t = 0$ , the edges support defective eigenvalues at zero energy. Similar behavior occurs for states localized on solitons (domain walls in the relative strength of  $t$  and  $J$ ), as we now discuss. As an example, we consider  $H^{(2,2)}$  in position space with open boundary conditions, with a domain wall as shown in Fig. 3(c). For clarity, we consider  $t > J$  and strong  $t$  bonds at the edges (as shown in Fig. 3(c)) so that the only localized states occur on the soliton, not at the edges [98, 99]. The energies of the states localized on the domain wall may be estimated by considering the limit  $J = 0$ . In this case, the energies are  $\epsilon = \pm\gamma\sqrt{1-u}$ . For  $u = 1$ , these are defective eigenvalues at zero energy with an algebraic multiplicity of two and a geometric multiplicity of one.

Numerical results are shown in Fig. 5 obtained by diagonalizing the Hamiltonian in position space with open boundary conditions, 802 orbitals in total, and a domain wall at the centre of the system. The complex energy spectra, top row of Fig. 5, look very similar to those of a fault-free system, bottom row of Fig. 4, the main difference is that the isolated energy levels are due to localized states on the domain wall instead of the ends. The bottom row of Fig. 5 shows the response power (25) as a function of  $u$ . There are plateaus at the location of the bands (on the real energy axis) and distinctive peaks corresponding to the edge states, with the most prominent peak appearing at zero energy for  $u = 1$ , similar to the behavior for edge states discussed in Sec. III B.

## IV. GRAPHENE

We consider monolayer graphene [75–77] as noninteracting fermions on the honeycomb lattice with nearest-neighbor hopping. This is another example of a parent model on a bipartite lattice with chiral symmetry, with the form of Eq. (2) where we replace  $h(k)$  with  $h(\mathbf{k}) = -\gamma_0 f^*(\mathbf{k})$  [76, 77, 100] where  $\gamma_0$  is the nearest-neighbor hopping parameter,  $\mathbf{k} = (k_x, k_y)$  is a two-dimensional wave vector, and

$$f(\mathbf{k}) = e^{ik_y a/\sqrt{3}} + 2e^{-ik_y a/(2\sqrt{3})} \cos(k_x a/2), \quad (43)$$

where  $a$  is the lattice constant.

We focus on the case of  $H^{(2,2)}$ , discussed for the SSH model in Sec. III D, which has two orbitals ( $A1$  and  $A2$ ) on every  $A$  site of the honeycomb lattice and two orbitals ( $B1$  and  $B2$ ) on every  $B$  site. This is similar to Fig. 3(b) where one can view the top and bottom layers as being honeycomb lattices, with hoppings  $t$  and  $J$  replaced by  $\gamma_0$ , and  $\gamma$  is an interlayer coupling appearing on every site. For an arbitrary degree of unidirectionality,  $0 \leq u \leq 1$ , we may use the formulae in Sec. III D, replacing

$h(k)$  with  $h(\mathbf{k})$ . A major difference as compared to the SSH model is that the band structure of the parent model is gapless whatever the parameter values, i.e.  $h(\mathbf{k}) = 0$  at the Dirac points in graphene.

The evolution of the complex energy spectra as a function of the degree of unidirectionality  $u$  is shown in Fig. 6. The top row shows energy eigenvalues determined numerically in position space with closed boundary conditions and 20000 orbitals. The middle row of Fig. 6 shows the real part of the energy bands and the bottom row shows their imaginary part, plotted using analytical formulae: dashed lines show the bands  $\epsilon_{r,\pm}(\mathbf{k})$ , Eq. (40), which are always real, and solid lines show the bands  $\epsilon_{i,\pm}(\mathbf{k})$ , Eq. (41), which are partly real and partly imaginary. The plots are for  $k_y = 0$  and  $-4\pi/3 \leq k_x a \leq 4\pi/3$ . This range includes two Dirac points at  $\mathbf{K}_\xi = \xi(4\pi/(3a), 0)$ ,  $\xi = \pm 1$ , in the parent monolayer graphene model where  $|h(\mathbf{K}_\xi)| = 0$ , and, at this point,  $\epsilon_{r,\pm}(\mathbf{K}_\xi)$  and  $\epsilon_{i,\pm}(\mathbf{K}_\xi)$  touch. For all plots, we use parameter values  $\gamma_0 = \gamma = 1.0$  for clarity of the qualitative features in the figures.

For bidirectional hopping  $u = 0$  (first column in Fig. 6),  $H^{(2,2)}$  is a nearest-neighbor hopping model of  $AA$ -stacked bilayer graphene [83, 84] which is Hermitian, and all the energy levels are real as given by Eqs. (35) and (36). There are two crossing points at zero energy where  $|h(\mathbf{k})| = \gamma$ . As  $u$  increases, the real bands  $\epsilon_{r,\pm}(\mathbf{k})$  (dashed lines) remain non-zero except for  $u = 1$  at the points where  $|h(\mathbf{K}_\xi)| = 0$ . Bands  $\epsilon_{i,\pm}(\mathbf{k})$  (solid lines) are generally partly real and partly imaginary, except for  $u = 1$  where they are imaginary (other than the points where  $|h(\mathbf{K}_\xi)| = 0$  and the energy is zero).

For  $u = 1$ , the energies are  $\epsilon_{r,\pm}(\mathbf{k}) = \pm\sqrt{\gamma|h(\mathbf{k})|}$  and  $\epsilon_{i,\pm}(\mathbf{k}) = \pm i\sqrt{\gamma|h(\mathbf{k})|}$ . Monolayer graphene has energies  $\pm|h(\mathbf{k})|$ , and  $H^{(2,2)}$  is a square root model [46, 50, 64–72] of it. Near the Dirac point of graphene,  $\mathbf{k} = \mathbf{K}_\xi$ , we consider a small wave vector  $\mathbf{q}$  as  $\mathbf{q} = \mathbf{k} - \mathbf{K}_\xi$  and  $f(\mathbf{k}) \approx -\sqrt{3}a(\xi q_x - iq_y)/2$  [76, 77] giving  $h(\mathbf{k}) \approx \hbar v(\xi q_x + iq_y)$  where velocity  $v = \sqrt{3}a\gamma_0/(2\hbar)$ . Thus, near the Dirac points, the Bloch Hamiltonian (4) is

$$\mathcal{H}^{(2,2)}(\mathbf{q}, 1) \approx \begin{pmatrix} 0 & 0 & 0 & Q^\dagger \\ \gamma & 0 & 0 & 0 \\ 0 & Q & 0 & 0 \\ 0 & 0 & \gamma & 0 \end{pmatrix}, \quad (44)$$

where  $Q = \hbar v(\xi q_x + iq_y)$ . This has energies  $\epsilon_{r,\pm}(\mathbf{k}) \approx \pm\sqrt{\gamma\hbar v|\mathbf{q}|}$  and  $\epsilon_{i,\pm}(\mathbf{k}) \approx \pm i\sqrt{\gamma\hbar v|\mathbf{q}|}$ , in agreement with Eq. (6). As discussed in Sec. II B, there is an exceptional point [13, 15–17, 27–43] at  $|\mathbf{q}| = 0$  where all eigenvalues are at zero energy with fourfold algebraic multiplicity, but twofold geometric multiplicity.

As with a trajectory around the Dirac point in the parent model, graphene [76–78], a trajectory in one of the bands enclosing the exceptional point acquires Berry phase  $\pi$ . To show this, we consider right  $|\psi_{R,\ell}\rangle$  and left  $|\psi_{L,\ell}\rangle$  eigenstates where  $\mathcal{H}^{(2,2)}(\mathbf{q}, 1)|\psi_{R,\ell}\rangle = \epsilon_\ell|\psi_{R,\ell}\rangle$ ,  $(\mathcal{H}^{(2,2)}(\mathbf{q}, 1))^\dagger|\psi_{L,\ell}\rangle = \epsilon_\ell^*|\psi_{L,\ell}\rangle$ , and  $\epsilon_\ell = i^\ell\sqrt{\gamma\hbar v|\mathbf{q}|}$  for

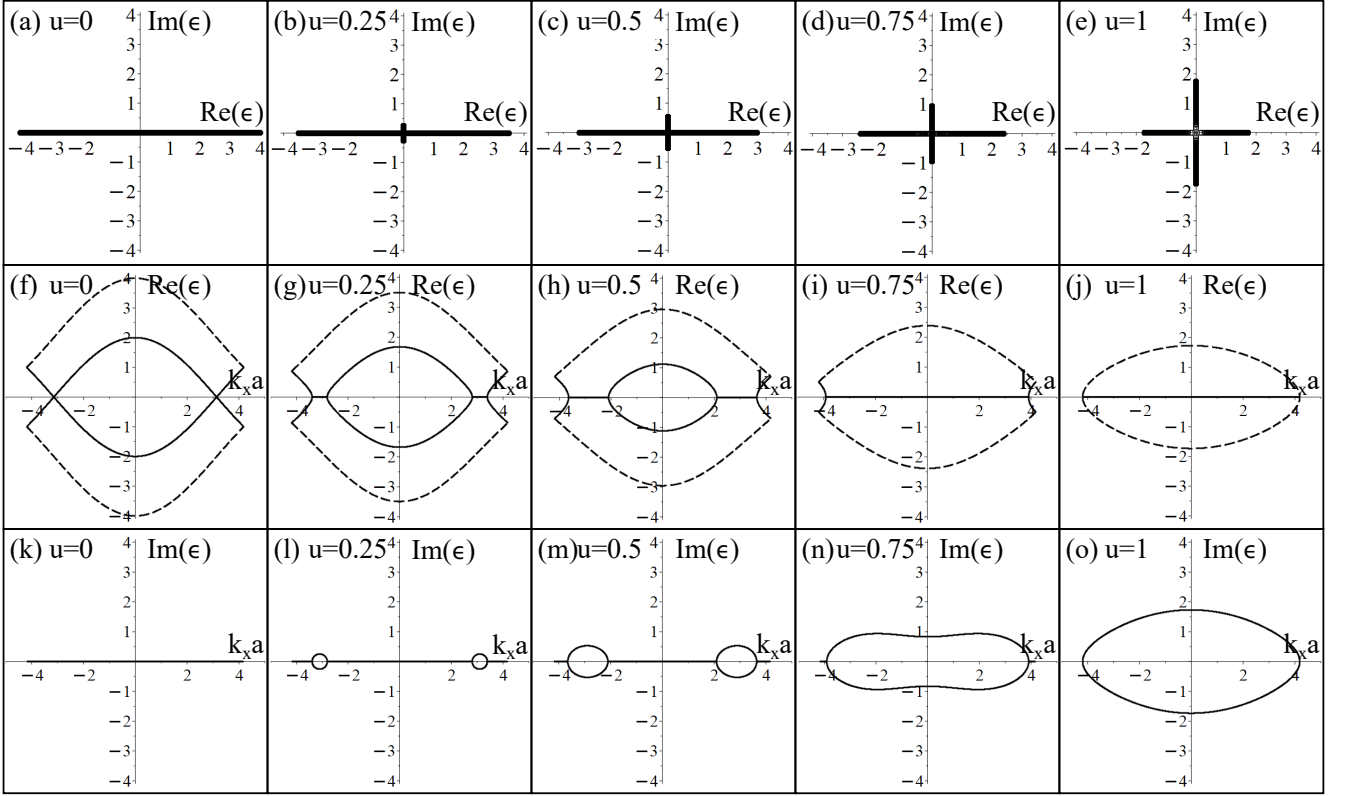


FIG. 6. Complex energy spectra for  $H^{(2,2)}$  with graphene as the parent model, as a function of the degree of unidirectionality  $u$ . The top row shows energy eigenvalues determined numerically in position space with periodic boundary conditions and 20000 orbitals. The middle row shows the real part of the energy bands and the bottom row shows their imaginary part, plotted for  $k_y = 0$  and  $-4\pi/3 \leq k_x a \leq 4\pi/3$ . Dashed lines show the bands  $\epsilon_{r,\pm}(k)$ , Eq. (40), which are always real, and solid lines show the bands  $\epsilon_{i,\pm}(k)$ , Eq. (41), which are partly real and partly imaginary. For all plots, parameter values are  $\gamma = \gamma_0 = 1.0$ .

$\ell = 0, 1, 2, 3$ . The left and right eigenstates are orthonormal as  $\langle \psi_{L,\ell} | \psi_{R,m} \rangle = \delta_{\ell,m}$ , and the complex Berry phase  $\Upsilon$  may be determined as  $\Upsilon = i \oint \langle \psi_{L,\ell} | \nabla_{\mathbf{q}} | \psi_{R,\ell} \rangle \cdot d\mathbf{q}$  [10, 79–82]. Taking a trajectory at constant  $|\mathbf{q}| > 0$  around the exceptional point, we find  $\Upsilon = \pi$  modulo  $2\pi$ , independent of the band index  $\ell$ .

These results can be generalized to  $H^{(n,n)}$ , the  $n$ th root model of monolayer graphene with  $p = 2n$  orbitals. For  $u = 1$ , and near the Dirac point of graphene, the  $p$  energy eigenvalues (6) are given by the complex solutions of  $(\epsilon_{\ell}^{(n,n)}(k, 1))^p = \gamma^{p-2}(\hbar v|\mathbf{q}|)^2$ . For  $|\mathbf{q}| = 0$ , there is an exceptional point as these eigenvalues are at zero energy with  $p$ -fold algebraic multiplicity, but twofold geometric multiplicity. A trajectory at constant  $|\mathbf{q}| > 0$  around the exceptional point acquires Berry phase  $\Upsilon = \pi$  modulo  $2\pi$ , independent of the band index  $\ell$ .

## V. CONCLUSIONS

We considered non-Hermitian Hamiltonians for non-interacting fermions with  $p$  orbitals per unit cell and unidirectional hopping, generated from parent Hermitian models on a bipartite lattice. For fully unidirectional

hopping, the models satisfy a complex version of chiral symmetry (1), and the  $p$  complex energy bands (6) are given by a common  $k$ -dependent real factor, determined by the bands of the parent model, multiplied by the  $p$ th roots of unity. When the SSH model is the parent model, the single-particle energy levels in position space (12) are the same as those of free parafermion solutions to Baxter's non-Hermitian clock model [44, 73, 74].

For fully unidirectional hopping, it is possible to generate an arbitrary  $n$ th root model (with  $p = 2n$  orbitals) of the parent model [46, 50, 64–72]. The models support exceptional points, with defective eigenvalues having an algebraic multiplicity of  $p$  and a geometric multiplicity of two. When the SSH model is the parent model, defective eigenvalues are realized in position space at edges with open boundary conditions and on solitons (domain walls in the relative hopping strength). When graphene is the parent model, defective eigenvalues occur at the corresponding Dirac points.

We described the role of partial unidirectional hopping, which breaks the complex chiral symmetry (1). With only real tight-binding parameters used throughout this paper, the models always satisfy time-reversal symmetry (14) which ensures that the energy spectrum is either real or comes with complex-conjugate pairs [85] (it

has reflection symmetry in the real energy axis). For an even number of orbitals  $p$ , the models also obey sublattice symmetry and the energy spectrum is either purely imaginary or comes with  $(\epsilon, -\epsilon^*)$  pairs [85] (it has reflection symmetry in the imaginary energy axis).

For fully bidirectional hopping, the constructed model is Hermitian, and it can be block diagonalized into even and odd parity blocks with respect to inversion of the orbitals within the unit cell. Partially unidirectional hopping breaks the inversion symmetry and mixes the even and odd blocks, and the real energy spectrum evolves into a complex one as the degree of unidirectionality in-

creases. This process is determined by the topology of the parent model and by the number of orbitals per unit cell,  $p$ , as we described in detail for  $p = 3$  and  $p = 4$  with the example of the SSH model. When the SSH model is the parent model, there are real energy levels due to states localized at the edges in the topological phase or on solitons.

## ACKNOWLEDGMENTS

The author thanks H. Schomerus for helpful discussions.

---

[1] W. P. Su, J. R. Schrieffer, and A. J. Heeger, Solitons in polyacetylene, *Phys. Rev. Lett.* **42**, 1698 (1979).

[2] W. P. Su, J. R. Schrieffer, and A. J. Heeger, Soliton excitations in polyacetylene, *Phys. Rev. B* **22**, 2099 (1980).

[3] J. K. Asbóth, L. Oroszlány, and A. Pályi, *A Short Course on Topological Insulators* (Springer, Switzerland, 2016).

[4] A. P. Schnyder, S. Ryu, A. Furusaki, and A. W. W. Ludwig, Classification of topological insulators and superconductors in three spatial dimensions, *Phys. Rev. B* **78**, 195125 (2008).

[5] A. Kitaev, Periodic table for topological insulators and superconductors, *AIP Conf. Proc.* **1134**, 22 (2009).

[6] S. Ryu, A. P. Schnyder, A. Furusaki, and A. W. W. Ludwig, Topological insulators and superconductors: ten-fold way and dimensional hierarchy, *New J. Phys.* **12**, 065010 (2010).

[7] C.-K. Chiu, J. C. Y. Teo, A. P. Schnyder, and S. Ryu, Classification of topological quantum matter with symmetries, *Rev. Mod. Phys.* **88**, 035005 (2016).

[8] C. M. Bender and S. Boettcher, Real Spectra in Non-Hermitian Hamiltonians Having PT Symmetry, *Phys. Rev. Lett.* **80**, 5243 (1998).

[9] Y. C. Hu and T. L. Hughes, Absence of topological insulator phases in non-Hermitian PT-symmetric Hamiltonians, *Phys. Rev. B* **84**, 153101 (2011).

[10] S.-D. Liang and G.-Y. Huang, Topological invariance and global Berry phase in non-Hermitian systems, *Phys. Rev. A* **87**, 012118 (2013).

[11] H. Schomerus, Topologically protected midgap states in complex photonic lattices, *Optics Letters* **38**, 1912 (2013).

[12] B. Zhu, R. Lu, and S. Chen, PT symmetry in the non-Hermitian Su-Schrieffer-Heeger model with complex boundary potentials, *Phys. Rev. A* **89**, 062102 (2014).

[13] S. Weimann, M. Kremer, Y. Plotnik, Y. Lumer, S. Nolte, K. G. Makris, M. Segev, M. C. Rechtsman, and A. Szameit, Topologically protected bound states in photonic parity-time-symmetric crystals, *Nature Materials* **16**, 433 (2017).

[14] M. Klett, H. Cartarius, D. Dast, J. Main, and G. Wunner, Relation between PT-symmetry breaking and topologically nontrivial phases in the Su-Schrieffer-Heeger and Kitaev models, *Phys. Rev. A* **95**, 053626 (2017).

[15] S. Lieu, Topological phases in the non-Hermitian Su-Schrieffer-Heeger model, *Phys. Rev. B* **97**, 045106 (2018).

[16] D. Halder, S. Ganguly, and S. Basu, Properties of the non-Hermitian SSH model: role of PT symmetry, *J. Phys.: Condens. Matter* **35**, 105901 (2023).

[17] C. C. Ye, W. L. Vleeshouwers, S. Heatley, V. Gritsev, and C. Morais Smith, Quantum metric of non-Hermitian Su-Schrieffer-Heeger systems, *Phys. Rev. Research* **6**, 023202 (2024).

[18] E. Slootman, W. Cherifi, L. Eek, R. Arouca, E. J. Bergholtz, M. Bourennane, and C. Morais Smith, Breaking and resurgence of symmetry in the non-Hermitian Su-Schrieffer-Heeger model in photonic waveguides, *Phys. Rev. Research* **6**, 023140 (2024).

[19] N. Hatano and D. R. Nelson, Localization Transitions in Non-Hermitian Quantum Mechanics, *Phys. Rev. Lett.* **77**, 570 (1996).

[20] N. Hatano and D. R. Nelson, Vortex pinning and non-Hermitian quantum mechanics, *Phys. Rev. B* **56**, 8651 (1997).

[21] N. Hatano and D. R. Nelson, Non-Hermitian delocalization and eigenfunctions, *Phys. Rev. B* **58**, 8384 (1998).

[22] S. Longhi, D. Gatti, and G. D. Valle, Non-Hermitian transparency and one-way transport in low-dimensional lattices by an imaginary gauge field, *Phys. Rev. B* **92**, 094204 (2015).

[23] S. Yao and Z. Wang, Edge States and Topological Invariants of Non-Hermitian Systems, *Phys. Rev. Lett.* **121**, 086803 (2018).

[24] F. Song, S. Yao, and Z. Wang, Non-Hermitian Topological Invariants in Real Space, *Phys. Rev. Lett.* **123**, 246801 (2019).

[25] J. S. Liu, Y. Z. Han, and C. S. Liu, Topological phases of a non-Hermitian coupled SSH ladder, *Chinese Phys. B* **28**, 100304 (2019).

[26] Y. Z. Han, J. S. Liu and C. S. Liu, The topological counterparts of non-Hermitian SSH models, *New J. Phys.* **23**, 123029 (2021).

[27] E. J. Bergholtz, J. C. Budich, and F. K. Kunst, Exceptional topology of non-Hermitian systems, *Rev. Mod. Phys.* **93**, 015005 (2021).

[28] J.-W. Ryu, J.-H. Han, C.-H. Yi, M. J. Park, and H. C. Park, Exceptional classifications of non-Hermitian systems, *Commun. Phys.* **7**, 109 (2024).

[29] T. Kato, *Perturbation Theory for Linear Operators* (Springer, New York, 1966).

[30] W. D. Heiss, Exceptional points of non-Hermitian operators, *J. Phys. A* **37**, 2455 (2004).

[31] M. V. Berry, Physics of non-Hermitian degeneracies, *Czech. J. Phys.* **54**, 1039 (2004).

[32] S. Klaiman, U. Günther, and N. Moiseyev, Visualization of Branch Points in PT-Symmetric Waveguides, *Phys. Rev. Lett.* **101**, 080402 (2008).

[33] W. D. Heiss, The physics of exceptional points, *J. Phys. A: Math. Theor.* **45**, 444016 (2012).

[34] K. Kawabata, T. Bessho, and M. Sato, Classification of Exceptional Points and Non-Hermitian Topological Semimetals, *Phys. Rev. Lett.* **123**, 066405 (2019).

[35] M.-A. Miri and A. Alu, Exceptional points in optics and photonics, *Science* **363**, eaar7709 (2019).

[36] J. Wiersig, Response strengths of open systems at exceptional points, *Phys. Rev. Res.* **4**, 023121 (2022).

[37] J. Wiersig, Distance between exceptional points and diabolic points and its implication for the response strength of non-Hermitian systems, *Phys. Rev. Res.* **4**, 033179 (2022).

[38] J. Wiersig, Petermann factors and phase rigidities near exceptional points, *Phys. Rev. Res.* **5**, 033042 (2023).

[39] S. Sayyad, M. Stålhammar, L. Rødland, and F. K. Kunst, Symmetry-protected exceptional and nodal points in non-Hermitian systems, *SciPost Phys.* **15**, 200 (2023).

[40] H. Schomerus, Eigenvalue sensitivity from eigenstate geometry near and beyond arbitrary-order exceptional points, *Phys. Rev. Res.* **6**, 013044 (2024).

[41] S. Bid and H. Schomerus, Uniform response theory of non-Hermitian systems: Non-Hermitian physics beyond the exceptional point, *Phys. Rev. Res.* **7**, 023062 (2025).

[42] J. Kullig, J. Wiersig, H. Schomerus, Generalized Petermann factor of non-Hermitian systems at exceptional points, arXiv:2506.15807

[43] S. Bid and H. Schomerus, Fragmented exceptional points and their bulk and edge realizations in lattice models, arXiv:2507.22158

[44] P. Fendley, Free parafermions, *J. Phys. A: Math. Theor.* **47**, 075001 (2014).

[45] A. M. Marques and R. G. Dias, Generalized Lieb's theorem for noninteracting non-Hermitian  $n$ -partite tight-binding lattices, *Phys. Rev. B* **106**, 205146 (2022).

[46] D. Viedma, A. M. Marques, R. G. Dias and V. Ahufinger, Topological  $n$ -root Su–Schrieffer–Heeger model in a non-Hermitian photonic ring system, *Nanophotonics* **13**, 51 (2024).

[47] S. Longhi, D. Gatti, and G. D. Valle, Robust light transport in non-Hermitian photonic lattices, *Scientific Reports* **5**, 13376 (2015).

[48] S. Weidemann, M. Kremer, T. Helbig, T. Hofmann, A. Stegmaier, M. Greiter, R. Thomale, and A. Szameit, Topological funneling of light, *Science* **368**, 311 (2020).

[49] C. Qin, B. Wang, Z. J. Wong, S. Longhi, and P. Lu, Discrete diffraction and Bloch oscillations in non-Hermitian frequency lattices induced by complex photonic gauge fields, *Phys. Rev. B* **101**, 064303 (2020).

[50] Z. Lin, S. Ke, X. Zhu, and X. Li, Square-root non-bloch topological insulators in non-hermitian ring resonators, *Opt. Express* **29**, 8462 (2021).

[51] S. Weidemann, M. Kremer, S. Longhi, and A. Szameit, Topological triple phase transition in non-Hermitian Floquet quasicrystals, *Nature* **601**, 354 (2022).

[52] Y. G. N. Liu, Y. Wei, O. Hemmatyar, G. G. Pyrialakos, P. S. Jung, D. N. Christodoulides, and M. Khajavikhan, Complex skin modes in non-Hermitian coupled laser arrays, *Light: Science & Applications* **11**, 336 (2022).

[53] Z. Gao, X. Qiao, M. Pan, S. Wu, J. Yim, K. Chen, B. Midya, L. Ge, and L. Feng, Two-Dimensional Reconfigurable Non-Hermitian Gauged Laser Array, *Phys. Rev. Lett.* **130**, 263801 (2023).

[54] S. Ke, W. Wen, D. Zhao, and Y. Wang, Floquet engineering of the non-Hermitian skin effect in photonic waveguide arrays, *Phys. Rev. A* **107**, 053508 (2023).

[55] X. Zhang, Y. Tian, J.-H. Jiang, M.-H. Lu, and Y.-F. Chen, Observation of higher-order non-Hermitian skin effect, *Nature Communications* **12**, 5377 (2021).

[56] H. Gao, H. Xue, Z. Gu, L. Li, W. Zhu, Z. Su, J. Zhu, B. Zhang, and Y. D. Chong, Anomalous Floquet non-Hermitian skin effect in a ring resonator lattice, *Phys. Rev. B* **106**, 134112 (2022).

[57] Z. Gu, H. Gao, H. Xue, J. Li, Z. Su, and J. Zhu, Transient non-Hermitian skin effect, *Nature Communications* **13**, 7668 (2022).

[58] J.-H. Wu, M. Artoni, and G. C. La Rocca, Non-Hermitian Degeneracies and Unidirectional Reflectionless Atomic Lattices, *Phys. Rev. Lett.* **113**, 123004 (2014).

[59] J. Li, A. K. Harter, J. Liu, L. de Melo, Y. N. Joglekar, and L. Luo, Observation of parity-time symmetry breaking transitions in a dissipative Floquet system of ultracold atoms, *Nat. Commun.* **10**, 855 (2019).

[60] T. Liu, Y.-R. Zhang, Q. Ai, Z. Gong, K. Kawabata, M. Ueda, and F. Nori, Second-Order Topological Phases in Non-Hermitian Systems, *Phys. Rev. Lett.* **122**, 076801 (2019).

[61] T. Hofmann, T. Helbig, C. H. Lee, M. Greiter, and R. Thomale, Chiral Voltage Propagation and Calibration in a Topoelectrical Chern Circuit, *Phys. Rev. Lett.* **122**, 247702 (2019).

[62] T. Helbig, T. Hofmann, S. Imhof, M. Abdelghany, T. Kiessling, L. W. Molenkamp, C. H. Lee, A. Szameit, M. Greiter, and R. Thomale, Generalized bulk–boundary correspondence in non-Hermitian topoelectrical circuits, *Nat. Phys.* **16**, 747 (2020).

[63] D. Zou, T. Chen, W. He, J. Bao, C. H. Lee, H. Sun, and X. Zhang, Observation of hybrid higher-order skin-topological effect in non-Hermitian topoelectrical circuits, *Nat. Commun.* **12**, 7201 (2021).

[64] J. Arkinstall, M. H. Teimourpour, L. Feng, R. El-Ganainy, and H. Schomerus, Topological tight-binding models from nontrivial square roots, *Phys. Rev. B* **95**, 165109 (2017).

[65] G. Pelegri, A. M. Marques, R. G. Dias, A. J. Daley, V. Ahufinger, and J. Mompart, Topological edge states with ultracold atoms carrying orbital angular momentum in a diamond chain, *Phys. Rev. A* **99**, 023612 (2019).

[66] M. Kremer, I. Petrides, E. Meyer, M. Heinrich, O. Zilbermanberg, and A. Szameit, A square-root topological insulator with non-quantized indices realized with photonic aharonov-bohm cages, *Nat. Commun.* **11**, 907 (2020).

[67] M. Ezawa, Systematic construction of square-root topological insulators and superconductors, *Phys. Rev. Research* **2**, 033397 (2020).

[68] A. M. Marques, L. Madail, and R. G. Dias, One-dimensional  $2^n$ -root topological insulators and superconductors, *Phys. Rev. B* **103**, 235425 (2021).

[69] B. Li, S. Qiu, L. Xu, S. Guo, R. Huang, and W. Qiu, Investigation of square-root higher-order topological insulator based on honeycomb-Kagome lattice of graphene plasmonic crystals, *Phys. Scr.* **99**, 1159100 (2024).

[70] H. Huang, M. Sarker, P. Zahl, C. S. Hellberg, J. Levy, I. Petrides, A. Sinitskii, and P. Narang, Topological Solitons in Square-Root Graphene Nanoribbons Controlled by Electric Fields, *Phys. Rev. Lett.* **134**, 256601 (2025).

[71] Y. Zhao, X. Zhang, Z. Cui, C. Wu, and N. Liu, Square-root topological insulator with high winding number, *Phys. Rev. B* **111**, 014109 (2025).

[72] L. Song, H. Yang, Y. Cao, and P. Yan, Realization of the square-root Dirac semimetal in electrical circuits, *J. Appl. Phys.* **137**, 124902 (2025).

[73] R. J. Baxter, A simple solvable  $Z_N$  Hamiltonian, *Phys. Lett. A* **140**, 155 (1989).

[74] R. J. Baxter, Superintegrable chiral Potts model: Thermodynamic properties, an “inverse” model, and a simple associated Hamiltonian. *J. Stat. Phys.* **57**, 1 (1989).

[75] K. S. Novoselov, A. K. Geim, S. V. Morozov, D. Jiang, Y. Zhang, S. V. Dubonos, I. V. Grigorieva, and A. A. Firsov, Electric Field Effect in Atomically Thin Carbon Films, *Science* **306**, 666 (2004).

[76] A. H. Castro Neto, F. Guinea, N. M. R. Peres, K. S. Novoselov, and A. K. Geim, The electronic properties of graphene, *Rev. Mod. Phys.* **81**, 109 (2009).

[77] E. McCann and M. Koshino, The electronic properties of bilayer graphene, *Rep. Prog. Phys.* **76**, 056503 (2013).

[78] M. V. Berry, Quantal phase factors accompanying adiabatic changes, *Proc. R. Soc. London, Ser. A* **392**, 45 (1984).

[79] H. Shen, B. Zhen, and L. Fu, Topological Band Theory for Non-Hermitian Hamiltonians, *Phys. Rev. Lett.* **120**, 146402 (2018).

[80] A. Fan, G.-Y. Huang, and S.-D. Liang, Complex Berry curvature pair and quantum Hall admittance in non-Hermitian systems, *J. Phys. Commun.* **4**, 115006 (2020)

[81] S. Tsubota, H. Yang, Y. Akagi, and H. Katsura, Symmetry-protected quantization of complex Berry phases in non-Hermitian many-body systems, *Phys. Rev. B* **105**, L201113 (2022).

[82] S. Longhi and L. Feng, Complex Berry phase and imperfect non-Hermitian phase transitions, *Phys. Rev. B* **107**, 085122 (2023).

[83] J.-K. Lee, S.-C. Lee, J.-P. Ahn, S.-C. Kim, J. I. B. Wilson, and P. John, The growth of AA graphite on (111) diamond, *J. Chem. Phys.* **129**, 234709 (2008).

[84] A. V. Rozhkov, A. O. Sboychakov, A. L. Rakhmanov, and F. Nori, Electronic properties of graphene-based bilayer systems, *Phys. Rep.* **648**, 1 (2016).

[85] K. Kawabata, S. Higashikawa, Z. Gong, Y. Ashida, and M. Ueda, Topological unification of time-reversal and particle-hole symmetries in non-Hermitian physics, *Nat. Commun.* **10**, 297 (2019).

[86] K. Kawabata, K. Shiozaki, M. Ueda, and M. Sato, Symmetry and Topology in Non-Hermitian Physics, *Phys. Rev. X* **9**, 041015 (2019).

[87] A. Mostafazadeh, Pseudo-Hermiticity versus PT Symmetry: The Necessary Condition for the Reality of the Spectrum of a Non-Hermitian Hamiltonian, *J. Math. Phys.* **43**, 205 (2002).

[88] D. Leykam, S. Flach, O. Bahat-Treidel, and A. S. Desyatnikov, Flat band states: Disorder and nonlinearity, *Phys. Rev. B* **88**, 224203 (2013).

[89] S. Flach, D. Leykam, J. D. Bodyfelt, P. Matthies, and A. S. Desyatnikov, Detangling flat bands into Fano lattices, *EPL* **105**, 30001 (2014).

[90] D. Leykam, A. Andreev, and S. Flach, Artificial flat band systems: from lattice models to experiments, *Adv. Phys. X* **3**, 677 (2018).

[91] C. Danieli, A. Andreev, D. Leykam, and S. Flach, Flat band fine-tuning and its photonic applications, *Nanophotonics* **13**, 3925 (2024).

[92] M. J. Rice and E. J. Mele, Elementary Excitations of a Linearly Conjugated Diatomic Polymer, *Phys. Rev. Lett.* **49**, 1455 (1982).

[93] R. T. Clay and S. Mazumdar, Cooperative Density Wave and Giant Spin Gap in the Quarter-Filled Zigzag Electron Ladder, *Phys. Rev. Lett.* **94**, 207206 (2005).

[94] X. Li, E. Zhao, and W. V. Liu, Topological states in a ladder-like optical lattice containing ultracold atoms in higher orbital bands, *Nat. Commun.* **4**, 1523 (2013).

[95] S. Cheon, T.-H. Kim, S.-H. Lee, and H. W. Yeom, Chiral solitons in a coupled double Peierls chain, *Science* **350**, 182 (2015).

[96] T. Zhang and G. B. Jo, One-dimensional sawtooth and zigzag lattices for ultracold atoms, *Sci. Rep.* **5**, 16044 (2015).

[97] C. Li, S. Lin, G. Zhang, and Z. Song, Topological nodal points in two coupled Su-Schrieffer-Heeger chains, *Phys. Rev. B* **96**, 125418 (2017).

[98] M. Inui, S. A. Trugman, and E. Abrahams, Unusual properties of midband states in systems with off-diagonal disorder, *Phys. Rev. B* **49**, 3190 (1994).

[99] R. E. J. Allen, H. V. Gibbons, A. M. Sherlock, H. R. M. Stanfield, and E. McCann, Nonsymmorphic chiral symmetry and solitons in the Rice-Mele model, *Phys. Rev. B* **106**, 165409 (2022).

[100] R. Saito, M. S. Dresselhaus, and G. Dresselhaus, *Physical Properties of Carbon Nanotubes* (Imperial College Press, London, 1998).